Journal of Colloid and Interface Science 611 (2022) 118–128

Contents lists available at ScienceDirect

Journal of Colloid and Interface Science

journal homepage: www.elsevier.com/locate/jcis

Improving superamphiphobicity by mimicking tree-branch topography

Wenwu Ding, Carlos Alberto Dorao, Maria Fernandino *

Department of Energy and Process Engineering. Norwegian University of Science and Technology, Trondheim 7491, Norway

GRAPHICAL ABSTRACT

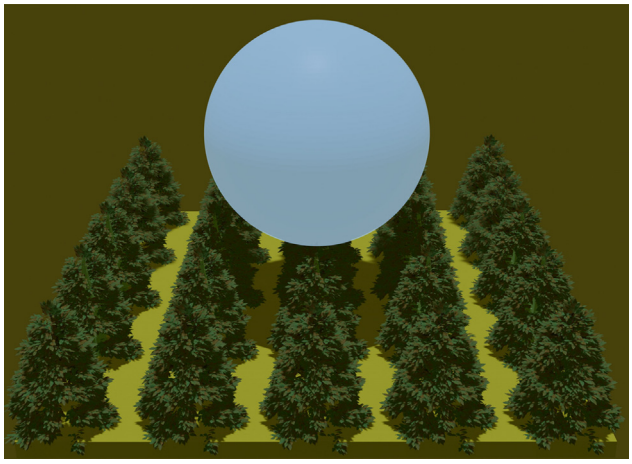

ARTICLE INFO

Article history:
Received 23 September 2021
Revised 7 December 2021
Accepted 8 December 2021
Available online 14 December 2021

Keywords:
Drop impact
Cones
Wetting
Adhesion
Surface tension
Superhydrophobic

ABSTRACT

when a droplet impacts on a superhydrophobic structured surface below a certain impact velocity, the droplet can bounce off completely from the surface. However, above such velocity a fraction of the droplet will pin on the surface. Surfaces capable of repelling water droplets are ubiquitous in nature or have been artificially fabricated. However, as the surface tension of the liquid is reduced, the capability of the surface to remain non-wetting gets hindered. Despite progress in previous research, the understanding and development of superamphiphobic surface to impacting low surface tension droplets remains elusive. It is proposed that multi-layer re-entrant like roughness can further enhance the anti-wetting properties also for low surface tension fluids.

In this work, we produce patterned conical micro-structures with lateral nano-sized roughness. Furthermore, the droplet impact experiments are conducted on various surfaces with variable surface tensions (27 mN/m - 72 mN/m) by using droplets with different Weber numbers (2–170).

We show that conical microstructures with lateral roughness mimicking tree-branches provides a surface topology capable of absorbing the force exerted by the droplet during the impact which prevents the droplet from pinning on the surface at higher impact velocity even for low surface tension droplets. Our study has significance for understanding the liquid interaction mechanism with the surface during the impact process and for the associated surface design considerations.

* Corresponding author.
E-mail address: maria.fernandino@ntnu.no (M. Fernandino).

https://doi.org/10.1016/j.jcis.2021.12.056
0021-9797/

1. Introduction

A superhydrophobic surface shows super-repellent properties presenting an apparent water contact angle above 150° and contact angle hysteresis below 10°. Thus, at low inclination angles millimeter-size droplets gently deposited roll off easily. In the case of structured surfaces, this low surface adhesion property is attributed to the air trapped below the droplet, allowing it to reach a Cassie-Baxter superhydrophobic state. Such super-repellent property also allows a droplet impacting on the surface bellow a certain impact velocity to bounce off completely from the surface. This property is essential for allowing the surface to remain clean without accumulation of droplet residue on the surface. Above a critical impacting velocity a fraction of the droplet will pin on the surface and the surface will favour the accumulation of liquid. Surfaces showing super-repelling properties to various fluids are crucial for multiple industrial and research fields such as microfluidics [1], drag reduction [2–6], self-cleaning surfaces [7–11], chemical shielding [12–14], antifouling [15–17], membrane processes[18–20], anti-fogging [21–24], anti-icing surfaces [25,26] and dropwise condensation [27–29]. Surfaces capable of repelling water droplets are ubiquitous in nature and have been artificially fabricated for multiple applications [30]. For example, a multi-fluorination surface design can show impalement resistance for water jet up to *We* number of 43000 [31]. Surfaces repelling low surface tension fluids (referred to as superamphiphobic) are also needed.

The most frequently used structure to keep a low surface tension droplet in superamphiphobicity state is re-entrant like structures [32–34,14]. This type of structure has a special top to pin the liquid, hence avoiding liquid penetration. Due to the complex fabrication process of re-entrant structures, modified re-entrant surfaces with easier production methods have been produced [35,36,12,37–40]. In addition, other types of nano structures or combination of micro/nano structures have also been reported to display superhydrophobic state for lower surface tension liquids [41–45].

However, it remains a challenge to produce a rigid surface capable of repelling low surface tension liquids impacting at high velocity. When a droplet impacts on a solid surface, there are different impact outcomes depending on the impacting velocity which is expressed in terms of Weber number ($We = \frac{\rho R V^2}{\gamma}$, ρ is liquid density, V is impact velocity, R is drop radius, γ is liquid surface tension.) At low Weber number, the droplet experiences either deposition or complete rebound. As the *We* number is increased, the droplet displays a partial rebound, receding break-up, prompt splash or corona splash [46]. Since a clean rebound is one of the expected properties for a super-repellent surface, the critical Weber number (when partial rebound starts to appear) should be considered together with the apparent contact angle, contact angle hysteresis and roll-off angle.

Nano-structures have been used in the literature to achieve better repelling capabilities of a surface by further enhancing the resistance to liquid impalement. In [41], the nano-scale fractal-like silica network surface shows a critical Weber number (complete rebound to partial rebound transition) around 4 to 40 for ethanol/water mixture droplets with 26–72 mN/m surface tension. Though nano-scale structures are able to increase the anti-wetting pressure here, the critical Weber number is not high. The authors suggest that there is deeper impalement of liquid inside the nano-network, resulting in partial rebound due to pinning of the impaled liquid at higher Weber numbers. In addition to nano structures, several works subsequently adopted micro-nano hierarchical structures to achieve clean rebound, as it is suggested that the micro/nano scale structures further reduce the solid–liquid contact area density but still have a high anti-wetting pressure. Dong et al. [42] report a critical Weber number in the range of 81–114 for surface tension of 24–28 mN/m, using a coating with hierarchical micro/nano scale roughness. Nevertheless, the surface used in their work has a tilting angle as high as 45° with respect to the horizontal surface. Note that the critical Weber number in [42] is defined as the maximum height condition at which the surface exhibits no permanent penetration, whereas the critical *We* number when partial rebound appears is not presented. Baek et al. [44] perform experiments of drop impact with liquid surface tension from 48–62 mN/m, reporting a critical Weber number ranging from 1 to 100 on their ZnO nanowires and ZnO/Si hierarchical structure surfaces. Ellinas et al. [43] achieve high critical impact velocity of 32-86 m/s, which leads to Wenzel state with the droplet facing downward. They use hierarchical micro-nano structured surfaces with defect-free hydrophobic coating for droplets with 66–36 mN/m surface tension. However, they do not report the critical *We* number for showing partial rebound. Different from the structure optimization method, Wong [47] uses surface chemistry enhancement to reach liquid super-repellency. Wong's work shows clean impact without liquid residue at *We* = 26 for droplets with surface tension of 27 mN/m. The proposed mechanism is the enhancement of the anti-wetting ability induced by the dense functionalized vertical network of fluoroalkyl on nanoparticles.

The previous mentioned works show that optimization of structures has to pose both high anti-wetting ability to resist impalement and also low solid–liquid contact area to have as low pining as possible. However, these two attributes can be conflicting, as a dense array has higher anti-impalement ability but results in higher adhesion due to increased solid–liquid contact. The reported nano or micro/nano structured surfaces show clean rebound of low surface tension droplets but in the Weber number range around 100 or below, which is still some distance to application requirements (some applications are involved with lower surface tension liquids and also *We* number larger than 100, for instance, inkjet printing [48–51] and liquid metal printing [52,53]). Therefore, it is necessary to further enhance the anti-wetting ability. Though surface tension and impact velocity are reflected in the *We* number, the resulting change of wettability due to change of surface tension is not represented here. Therefore, the critical *We* number and surface wettability properties should be quantified together.

In order to have a clean rebound, the energy dissipation during droplet impact has to be minimized. The initial spreading phase of drop impact is driven by kinetic energy, and part of the energy is lost in viscous dissipation and part converted into surface energy. From the receding phase, the surface energy stored in the droplet deformation drives the receding with part of the energy converted into kinetic energy and part lost to viscous dissipation. In addition to viscous dissipation, energy dissipation at the contact line is shown to affect drop impact dynamics as well [54–56]. Therefore, the design of structures should achieve minimization of viscous energy dissipation and energy dissipation at the contact line. In this direction, it has already been shown that increased hierarchical level can enhance the anti-wetting behavior during drop impact [44,43,57]. In [57] they propose that the solid–liquid contact fraction is further reduced by increasing the hierarchical level while the anti-wetting capillary pressure is also increased due to the nano-structure. Additionally, the micro structures of hierarchical surfaces reduce liquid compression related pressure when the liquid penetrates into the micro structures [58]. In Pan et al.'s [35] work, they report non-wetting of pentane at Weber number of 250 using multi-re-entrant hierarchical structured woven fabric surfaces. However, the sample itself is soft and moving during impact, thus the impact energy is not only stored in the droplet deformation but also in the solid material deformation. This Weber number is currently the highest found for this range of liquid

surface tension, implying that an increased level of re-entrant structures is beneficial for superrepellency of lower surface tension droplets at higher Weber number.

However, the reported robust superamphiphobic structures with re-entrant like roughness [42,35] are randomly built, which hinders investigation of dominant design parameters. Previous works have shown that conical structures lead to low adhesion [59,60] and withstand certain drop impact energy up to *We* = 1785 for water droplets [61]. In this work, we make a step further and produce patterned micro-conical structured surfaces with re-entrant like lateral wall roughness, which mimics a tree-branches topology. The tree-branches like structures relax the conflicting role of anti-impalement ability and adhesion properties to some extent, where the essential role of lateral roughness is experimentally illustrated in the current work.

2. Experimental method

The conical structured surfaces are produced using well-known photo-lithography and etching techniques as described in previous work [59]. The general sample fabrication process is shown in Fig. 1. A raw silicon wafer is at first cleaned by acetone, ethanol, 2-propanol and de-ionized water, after which the wafer is dried by nitrogen flow. Then the clean wafer is coated with negative photoresist Mr-DWL5, which is used as etching mask. The design pattern is an array of circles with 1 micrometer in diameter placed in square arrangement with different center to center pitch distance on the same wafer (with pitch of $\sim 3\mu m, \sim 5\mu m, \sim 8\mu m$ and $\sim 10\mu m$). To produce this resist pattern array, we expose the resist layer using 405 nm wavelength laser from a maskless aligner MLA 150 and develop this resist layer in developer Mr-Dev 600. When the resist pattern array is prepared, we etch into the silicon surface to produce silicon pillars using an Oxford Cryo ICP-RIE dry etching device. By using different etching parameters, we produce smooth conical structures and cones with horizontal oriented side wall roughness. The resist on the sample after etching is removed using oxygen and CHF_3 plasma. In Fig. 1, we show the smooth conical structures and the side wall roughened conical structures with pitch 3 μm. The intrinsic wetting property is changed to hydrophobic by coating the samples with silane. The etching parameters for smooth cones were: etching temperature of -50°C in a SF_6/O_2-85/16 sccm gas at a pressure of 30 mTorr for 14 min, then O_2 plasma for 10 min (15 mTorr, 40 sccm) and CHF_3 plasma for 5 min (20 mTorr, 50 sccm). The etching parameters for cones with sidewall roughness were:

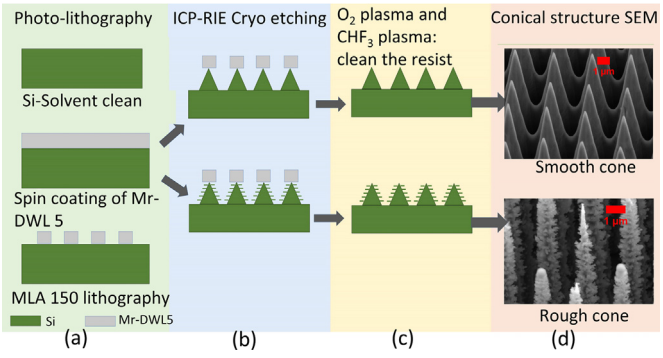

Fig. 1. Schematic fabrication process. The micro-conical structured silicon surfaces are produced using photo-lithography and dry etching. In (a), photo-lithography process, including solvent cleaning, spin coating of resist, resist exposure and development. In (b), the plasma etching process is shown, where the side wall property is controlled by the etching parameters. In (c), the resist clean process is illustrated. In (d), we show the scanning electron microscope (SEM) image for cones with smooth and roughened side wall.

etching temperature of -100°C in a SF_6/O_2-85/11 sccm gas at a pressure of 20 mTorr for 26 min, then N_2 gas flow for around 30 min, followed by 10 min O_2 plasma (15 mTorr, 40 sccm) and 5 min CHF_3 plasma (20 mTorr, 50 sccm). The sidewall roughness is mainly formed during the N_2 gas flow step.

Droplets with different surface tension are produced by mixing ethanol and de-ionized water in different volume ratios. The droplet impact process is recorded using a Photron Fastcam SA3 camera with 500 frames per second at ambient conditions to see the droplet bouncing, and 4000 frames per second when measuring contact time. A dispenser can produce droplets falling down vertically onto the sample surface with volume around 4–11 μl. A vertical stage can be moved up and down to adjust the impact speed. Contact angle is measured using an optical tensiometer from Biolin Scientific at ambient conditions. A droplet with volume 3.5–8 μl is gently deposited onto the sample, then the sample stage is tilted and the surface static contact angle and tilting angle can be quantified. From repeating experiments, the error (standard deviation) range of surface tension (27 mN/m - 72 mN/m) is (1 mN/m - 2 mN/m), the error range of static contact angle (90°-175°) is (1°-5°), the error range of silidng angle (0.4°-90.0°) is (0.1°-5.0°), and the error range of critical Weber number (0–151) is (1–4).

3. Results and discussions

3.1. Contact angle and sliding angle

At first, we characterize the static contact angle and sliding angle using an ethanol/water mixture. We deposit the droplet gently and record the contact angle and tilting angle while tilting the sample stage. For simplicity, the following notation will be used to refer to the different surfaces: RP3H27 is the abbreviation for rough (R) conical structure with pitch (P) 3μm and height (H) $\sim$27μm. SP3H20 is the abbreviation for smooth (S) conical structure with pitch (P) 3μm and height (H) $\sim$20μm. The same nomenclature is used for the other samples. The smooth conical sample is around $\sim$20 μm high, while the cones with sidewall roughness are around $\sim$27 μm in height. In Fig. 1, and Fig. 2(b), we show the static contact angle and sliding angle for all the produced samples. In Fig. 2(a), we also show the static contact angle on a flat hydrophobic silicon surface. Among all the mixture cases, hydrophobic wetting state is observed for surface tension above 45 mN/m and hydrophilic below 45 mN/m on the flat cases. Fig. 2(a) displays the static contact angle vs. surface tension. In general, the static contact angle decreases when surface tension is lower for all surfaces. However, different surface tension ranges result in different contact angle for rough or smooth cones. When the surface tension is larger than 37 mN/m (green patch), both rough and smooth cones show similar contact angle (less than 6° difference). The red patch range (γ smaller than 37 mN/m) exhibits a more distinct difference (more than 16° difference) of contact angle between the rough and smooth cones. In particular, the rough cones (pink patch) all have higher contact angle than the smooth cones (blue patch) in this range. Based on the Cassie-Baxter model these results indicate that the sidewall roughness reduces the solid–liquid contact area density in this lower surface tension range, but the effect of the sidewall roughness on the solid–liquid contact area density is small when the surface tension is higher. We propose that the effect of the sidewall roughness appears when partial or full liquid penetration happens, since otherwise the sidewall roughness effect should be negligible for rough and smooth cones of the same pitch. For all the surface tension range tested, the contact angle difference among rough cones for different pitch cases is small (less than 3° difference in the green patch, and less than 5° difference in the red patch). In Table 1, the solid–liquid fraction

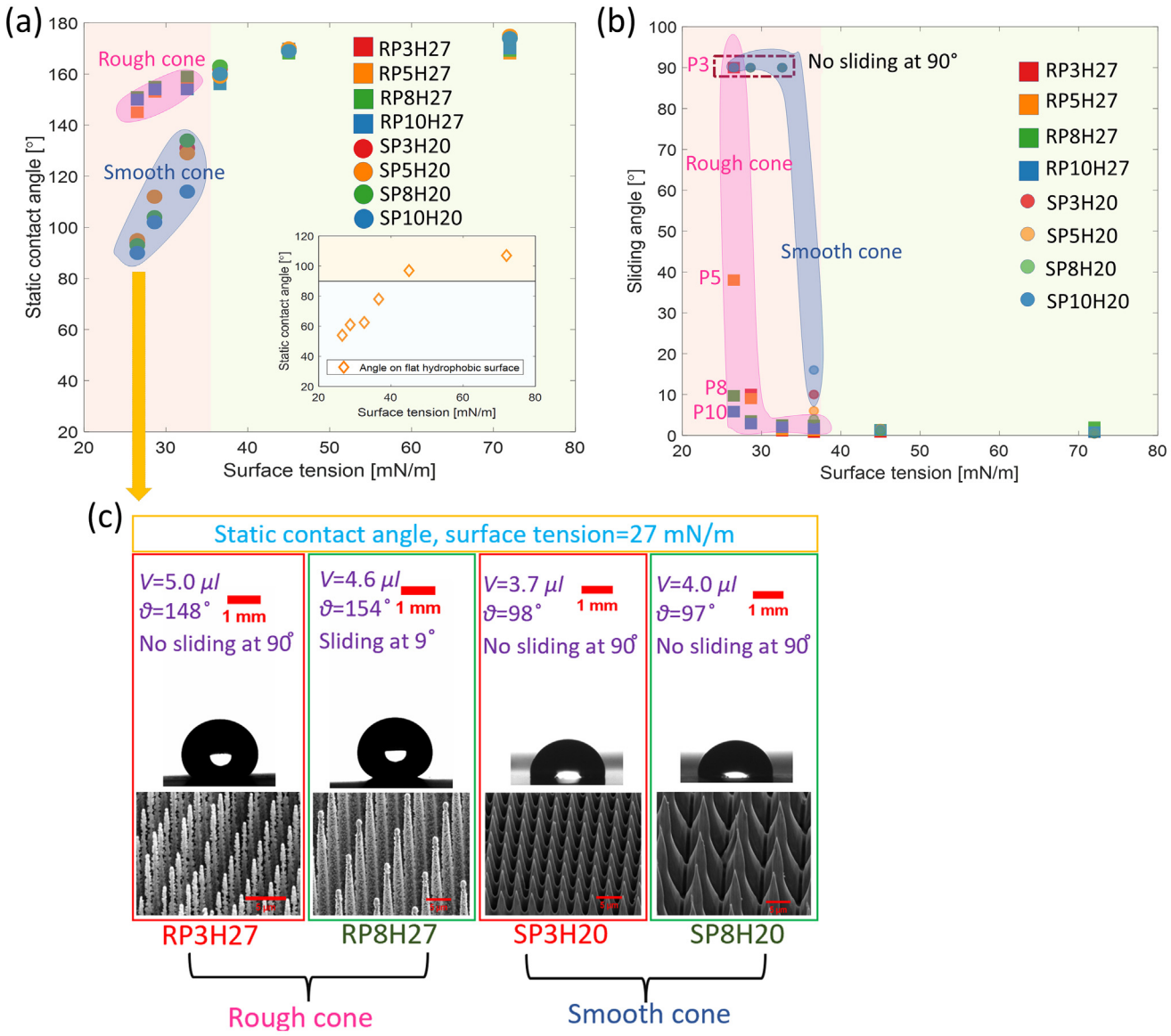

Fig. 2. Wetting property characterisation. In (a), static contact angle vs. surface tension on 8 conical surfaces are shown. In general, the angle is decreasing slightly with lower surface tension. The static contact angle on a flat hydrophobic surface is presented as well, which reflects the intrinsic contact angle for different types of ethanol mixtures droplet. In (b), the sliding angle is plotted against surface tension. It is shown that when the surface tension is roughly below 30 mN/m, the hysteresis starts to increase distinctively, which suggests that the solid–liquid contact is increased even at the static case for lower surface tension droplets. Cones without side wall roughness display similar or higher sliding angle. In (c), snapshots of the sessile droplet sitting on two types of surfaces are presented for pitch 3 μm and pitch 8 μm.

$\psi = \pi d^2/4P^2$, where d is the structure top diameter and P is the pitch, and contact angle for water from pitch 3 μm to pitch 10 μm are presented. The solid fraction is around 0.005 to 0.013 and the contact angle ranges from 172°-177°. The small solid fraction difference corresponds to contact angle differences of 5° maximum between pitch 10 μm to pitch 3 μm based on the Cassie-Baxter equation. Therefore, the small static contact angle difference is expected for rough cones. However, the smooth cones show larger contact angle difference for different pitch (up to 20° difference when γ is smaller than 37 mN/m), which suggests that smooth cones are not in the Cassie-Baxter state due to partial liquid penetration. A larger pitch for the smooth cones leads to lower contact angle, implying more solid–liquid contact based on the Cassie-Baxter mode, which is proposed to be induced by more penetration into the structures.

Table 1
Surface solid fraction and predicated contact angle.

Surface	Solid fraction	Contact angle based on Cassie-Baxter equation [°]
RP3H27	0.013	172
RP5H27	0.005	175
RP8H27	0.007	174
RP10H27	0.005	175
SP3H20	0.013	172
SP5H20	0.005	175
SP8H20	0.002	177
SP10H20	0.001	177
Flat surface	1	107

Fig. 2(b) shows the sliding angle vs. surface tension for the same cases. Generally, the sliding angles in the hydrophobic range (green patch) are all similar (less than 2° difference) and small around 0°, while the sliding angle starts to increase when surface tension (red patch) decreases. Inside this red patch range, the rough cones (enclosed in pink patch) show lower sliding angle compared with

smooth cones (enclosed in blue patch). When surface tension is above 30 mN/m, the sliding angle is around zero for all conical samples with lateral roughness, but the sliding angle starts to increase below 30 mN/m. At γ = 27mN/m, RP8H27 and RP10H27 still have low sliding angle (below 10°), while RP3H27 and RP5H27 have larger sliding angle (above 35°). RP3H27 shows no sliding even at 90° tilting, indicating that a smaller pitch leads to higher adhesion. However, in the same red patch range, the smooth cones have sliding angle above 5° when γ = 37 mN/m and display no sliding when γ is lower than 32 mN/m. Based on the difference observed between rough and smooth cones, it is found that smooth cones have larger adhesion and we attribute this to liquid penetration. The rough cones resist penetration better and result in less actual solid–liquid contact area, and therefore a lower threshold for depinning.

Fig. 2(c) presents the images of droplets with surface tension γ = 27 mN/m gently deposited onto the surfaces with pitch 3 μm and 8 μm. The two rough conical cases have larger contact angle than the smooth cones with the same pitch. For the two smooth cones, the contact angle is around 97°, which is far from the Cassie-Baxter equation prediction (larger than 160°). The penetration induced large solid–liquid contact area increases the smooth cones surface adhesion resulting in no droplet sliding. For RP3H27, the contact angle is around 148° but still no sliding is observed. We attribute this to the dense array of the structure, which leads to larger solid–liquid contact area density and thus higher adhesion. In addition, there may exist partial liquid penetration resulting in more pinning, which in turn increases the adhesion further. Among the four cases, only RP8H27 shows sliding angle at around 9° while other cases have no sliding at 90°, implying that proper design of the sidewall roughness and pitch has the potential to reduce the surface adhesion.

3.2. Enhanced anti-wetting at higher Weber number

Here the rough conical surface repelling capabilities are tested at higher *We* number. The drop impact experiments are performed using low surface tension droplets. The micro cones with sidewall roughness have a similar cone height of $\sim 27\mu m$, with 4 pitch designs respectively (SEM shown in Fig. 3(a)). Fig. 3(c) displays high-speed snapshots of a $\sim 2mm$ diameter droplet with surface tension of 37 mN/m impacting on the RP8H27 surface for two different *We* numbers. In both cases, the droplet shows first a spreading regime until reaching a maximum spreading, from where it starts receding and finally bounces back from the surface. However, the higher *We* number case shows longer vertical stretching and a liquid residue after rebound. Fig. 3(c) exhibits the advancing phase in the first three snapshots. The droplet will increase the surface area by thinning and spreading to the maximum contact diameter. In the receding phase from the fourth snapshot, the deformed thinner liquid starts to reduce the solid–liquid contact and increases the liquid vertical stretch. Finally, the liquid can go upward. The receding process is driven by energy stored in droplet deformation with part of the energy converted to kinetic energy and part lost into viscous dissipation and energy dissipation at the contact line. But the outcome of the receding phase varies for the two cases shown. For the lower impacting *We* number case, the droplet shows a total rebound with a small vertical droplet stretching before leaving the surface. Regarding the higher *We* number case, the vertical stretching during the final detachment stage is increased and a small liquid residue is left on the surface after the rebound. At increased *We* number, it is more strenuous for the droplet to bounce away from the same surface.

From an energy point of view, a complete rebound can happen when the droplet energy just before the rebound is just above a certain droplet energy threshold equal to the surface energy of the spherical droplet according to [62]. A clean rebound at lower impact We therefore means the remaining droplet energy is larger than the threshold droplet energy, while the higher impact *We* case is contrary. As shown in Fig. 3(c), at impact *We* number of 170, the liquid is stretched more with the presence of a liquid residue, compared with *We* = 6. This is caused by the increased energy dissipation, which can be induced by penetration of the liquid into the structures.

When the critical impact velocity is reached, the impact outcome will be partial rebound as shown in Fig. 3(c). The critical Weber number is defined as, $We = \frac{\rho R V_c^2}{\gamma}$, with V_c the critical velocity at which a partial rebound starts to appear when increasing the impact height. Here, we use the critical *We* number to compare the repelling performance between different surfaces. The data is summarized in Fig. 3(b). Reference data from two previous works [41,44] are also included. For surface tension of 45 mN/m, the RP10H27 surface reaches the critical Weber number while all other surfaces show no liquid residue even at Weber number around 151. For pure water, all surfaces show complete rebound at the maximum impact velocity. In the hydrophobic range, the surface tends to repel the liquid hence resisting liquid penetration. More impact energy is needed in order to push the liquid into the structure [63,64]. For the hydrophilic case, the liquid has lower surface tension and therefore the liquid tends to wet the surface. At surface tension of 27 mN/m, surfaces RP3H27 and RP5H27 are not capable of reaching a complete rebound whereas only RP8H27 and RP10H27 show complete rebound. One possible reason is the penetration difference and the solid–liquid contact adhesion difference. The lower pitch samples are denser and thus more difficult to penetrate but the solid–liquid contact area is larger resulting in higher adhesion, which is in agreement with the contact angle and sliding angle data. Additionally, the pillar top shape affects the local penetration ability. The larger top cases (surfaces RP8H27 and RP10H27 have a larger pillar top here) resist penetration better [65,66]. For surface tension of 37 mN/m, RP8H27 shows best performance, which is due to the effect of lower solid–liquid contact adhesion as well as sufficient anti-wetting pressure. RP8H27 and RP10H27 resist penetration better due to larger pillar top [65,66]. Plus there is lower solid–liquid contact area density for the higher pitch cases. As a result, the pitch 8 μm and 10 μm cases display higher anti-impalement ability. With a similar type of pillar top, surface RP8H27 is better due to the denser array, which leads to a higher anti-wetting pressure.

For the intrinsic hydrophilic case, to achieve a non-wetting state the side wall roughness structure has to be designed to satisfy certain requirements. For instance, the liquid intrinsic contact angle has to be larger than the angle between the tangent of the structure highest point with the horizontal symmetry axis [63]. The shape of the sidewall structure leads to different local breakthrough pressure [67]. In our work, the surface has lateral roughness all along the pillar (it can be taken as a multi layer sidewall structure), which is possibly one of the reasons why the repelling ability is enhanced. For the lower pitch case, the surface has more pinning sites to resist the liquid penetration, but at the cost of higher solid–liquid adhesion to overcome during rebounding. It is the opposite trend for higher pitch samples. Thus there may exist an optimum design for both enough anti-wetting ability and comparatively lower solid–liquid adhesion. In summary, the enhanced performance is related with the sidewall roughness and the solid–liquid contact adhesion property.

3.3. Important role of lateral roughness

To further confirm that the side wall roughness plays a dominant role, the critical *We* number is compared for smooth cones

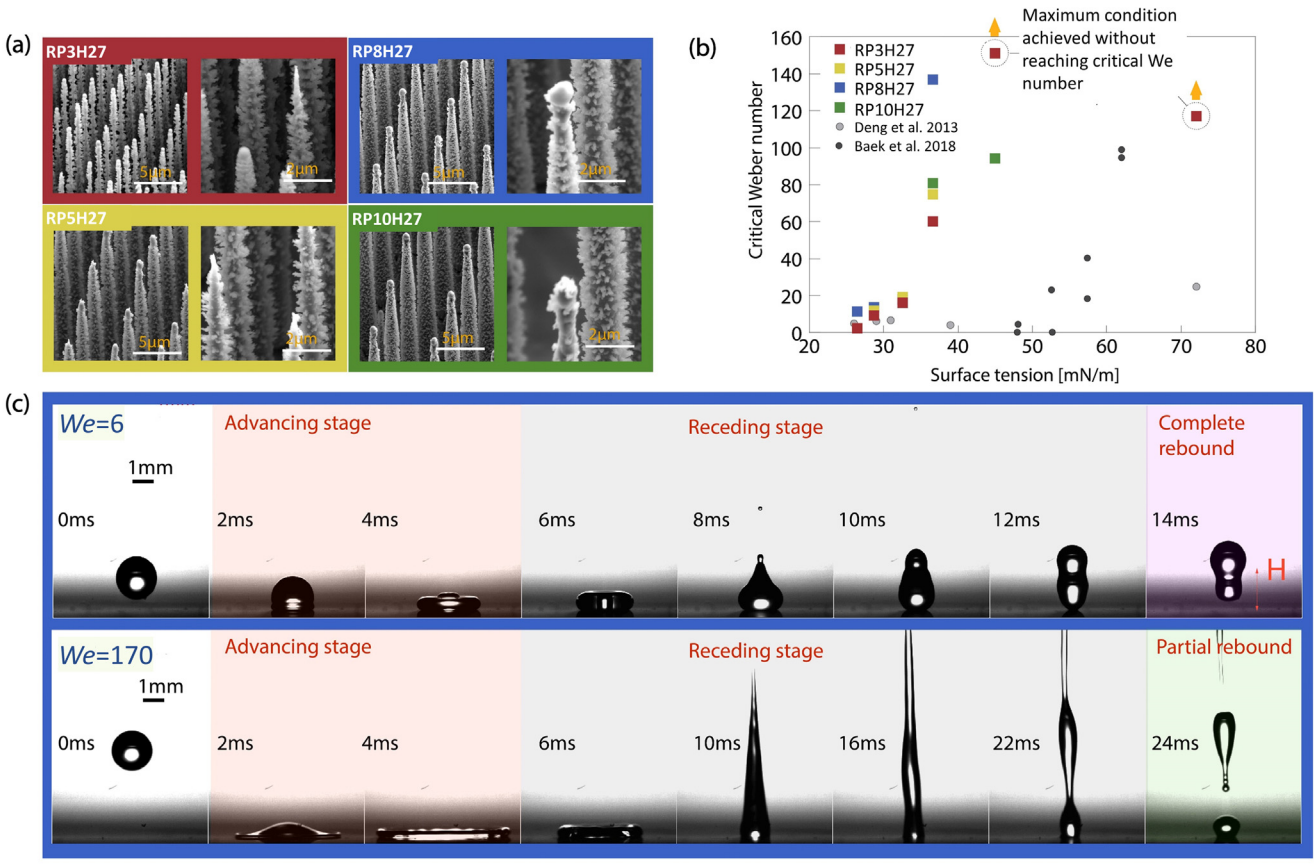

Fig. 3. (a) Scanning electron microscope images of conical micro-structures with side wall roughness. (b) The critical Weber number vs. surface tension on surfaces with side wall roughness is presented. Compared with data from two references [41,44], the structures in this work have distinct higher critical Weber number in the surface tension range of 36–72 mN/m. The critical Weber number in the range 26–32 mN/m also shows certain improvement. The cases enclosed in dash circle mean the conditions shown has not reached the critical We number yet. (c) Drop impact at *We* = 6 and *We* = 170, showing complete rebound and partial rebound respectively, using droplets of surface tension of 37 mN/m and. surface RP8H27.

(SEM presented in Fig. 4)) and rough cones and is plotted in Fig. 4 (b). Three types of liquids with equilibrium angle (θ_E) of 54° (surface tension 27 mN/m), 63° (surface tension 33 mN/m) and 78° (surface tension 37 mN/m) are used in the comparison. It is observed that smooth cones have distinct lower critical Weber number as compared with cones with lateral roughness. This is further shown in Fig. 5, showing the critical Weber number with the corresponding critical Reynolds number ($Re = \frac{\rho RV}{\mu}$, ρ is liquid density, V is impact velocity, R is drop radius, μ is liquid dynamic viscosity). It is observed that smooth cones (in blue patch) have distinct lower critical Weber number and critical Reynolds number

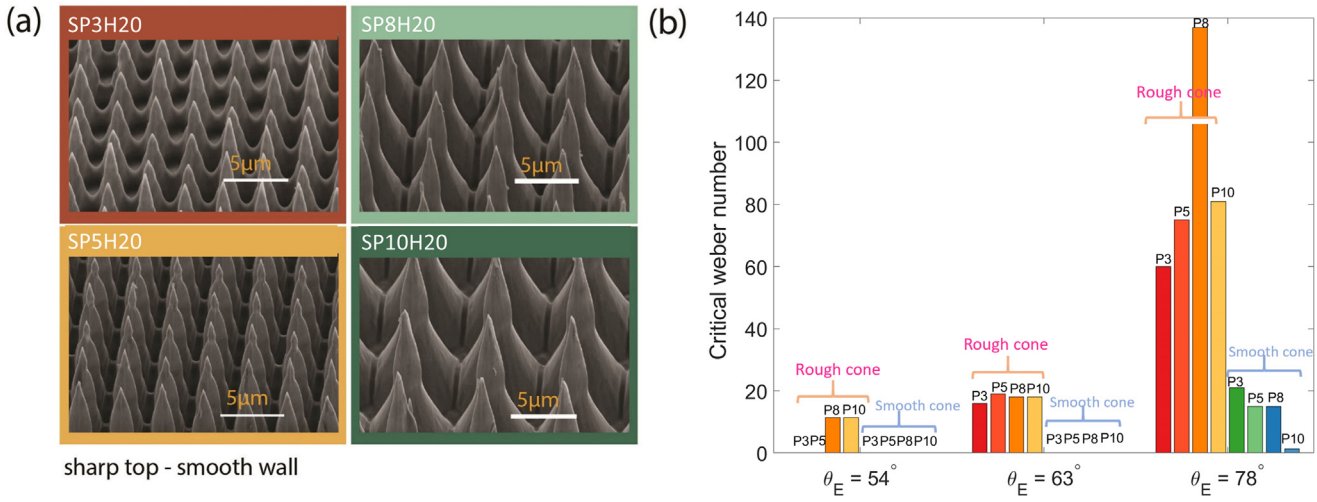

Fig. 4. (a) SEM of conical micro-structures without side wall roughness. In (b),critical Weber number vs. surface tension on surfaces with and without side wall roughness. Cones without side wall roughness show distinct lower critical Weber number.

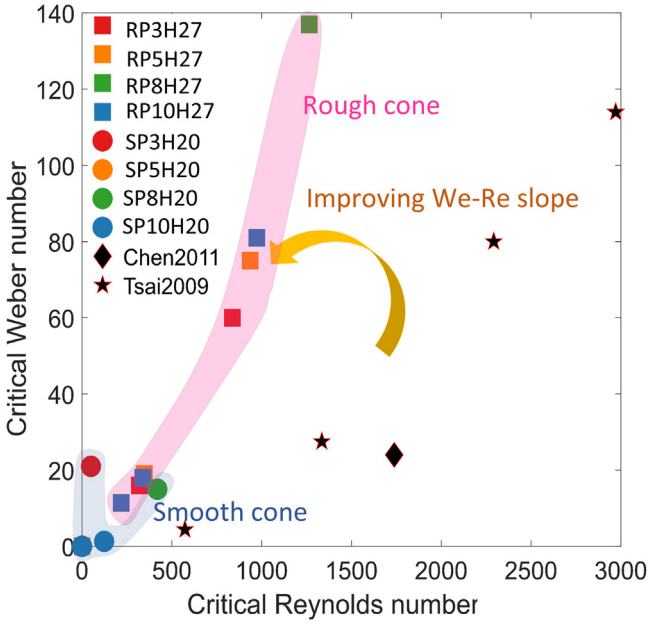

Fig. 5. Critical Weber number from Fig. 4(b) is plotted vs. critical Reynolds number. Three surface tension cases (27 mN/m, 33 mN/m, 37 mN/m) on surfaces with and without side wall roughness are compared. Two reference data sets [68,69] for water droplet impact are also adde.d in the figure.

compared with cones with lateral roughness (in pink patch). The We-Re number data points for water droplets when partial rebound start to appear from Chen et al.'s [68] and Tsai et al.'s work [69] are shown in the same plot. The nano-grass surfaces [68] and micro-structured surfaces [69] in these two works have lower critical Weber number. This plot further demonstrates that the surfaces designed in this work improve the anti-wetting ability even when using lower surface tension liquids.

In the first two rows of Fig. 6(a), for γ = 27 mN/m, there is no rebound (shown in last image in blue patch) on smooth cones with pitch 8 μm (the SEM image was shown in Fig. 4(a)) but we have complete rebound on cones with lateral roughness with pitch 8 μm at We = 7. In the last two rows of Fig. 6(a), we use drops of surface tension 45 mN/m on the two types of surfaces. Cones without lateral roughness here start to show partial rebound (shown in last image in red patch) while the cones with lateral roughness display complete rebound at We = 33.

Previous works have proposed structures with lateral roughness as optimum structures theoretically as they can increase the breakthrough pressure [63,64]. Adding sidewall roughness [70] and design of the sidewall structure shape will alter the local breakthrough pressure [67]. From the pressure balance point of view, the sidewall roughness can increase the breakthrough pressure. This is also true from an energy perspective. If the structure has no sidewall roughness, the energy barrier between Cassie state and Wenzel state will be smaller than the case with sidewall roughness [63]. As shown in literature, a multi-layer structure (ripple shape) has various intermediate energy stable states [71–73], which means that there exists multiple, successive energy barriers when the liquid penetrates into the structure, making this type of structure beneficial to avoid a direct Cassie-Wenzel transition. In addition, the sidewall structure shape plays different roles by controlling how the liquid advances on the side wall [67], which can affect the anti-wetting ability. Our structures are conical pillars with horizontal oriented lateral roughness all along the side wall, which can be described as N layers of horizontal oriented lateral structures on the side wall, similar as tree-branches. When the liquid penetrates one layer of this structure, its impact energy will be reduced due to the solid–liquid contact adhesion. If the wetting pressure from the reduced impact energy is smaller than the local breakthrough pressure, the liquid will stop further penetration. If the wetting pressure is still higher than the local breakthrough pressure, the liquid can continue penetration and more layers of the structures will be wetted until the wetting pressure is smaller than the breakthrough pressure.

We schematically show the resulting solid–liquid contact for smooth cone and roughed cone in Fig. 6(b). In the hydrophobic case, the rough cones, with either bigger top or sharper top, can maintain low penetration and thus smaller solid–liquid contact, while the smooth cones have much higher penetration and thus larger solid–liquid contact. In the hydrophilic case, we propose that the rough cones with larger top can keep smaller penetration level as compared with rough cones with sharper top or smooth cones, due to higher capillary force and also more edge pinning effect. Actually, previous works show that design of an under-cut profile can be beneficial for superhydrophobicity [74,32,33,40], where among the design criteria, the structure top shape is a key parameter. A re-entrant angle [33,34,65] or double re-entrant structures [75,36] have also been suggested. Our work provides new insight that a multi-layer under-cut profile consisting of a horizontal oriented lateral roughness can also improve the superhydrophobicity by resisting penetration in a better way in the tested low surface tension range.

3.4. Bouncing process

To reveal further how the different surfaces respond to drop impact at the same velocity, we show more details of the rebound process. We deposit the droplet from around 1 cm height and record the rebound process. Fig. 7(a) presents the bouncing process with time, showing the droplet center position variation with time. The droplet center position is obtained using Matlab image processing. We use surface RP8H27 as substrate and deposit a single droplet with different surface tension. Three types of droplets are shown in this plot, including pure water, ethanol water mixtures with surface tension of 37 mN/m and 27 mN/m. The number of rebounds and first bouncing height is decreasing with decreasing surface tension, though Weber number is similar. This indicates that energy is dissipated more for lower surface tension droplets. As the surface is the same, the reason is suggested to be the actual solid–liquid contact area difference due to temporary impalement (as the ethanol/water mixtures viscosity has less than 0.001 Pa.s difference [76] in these cases, viscosity difference plays a minor role). The lower surface tension case has more solid–liquid contact which results in more adhesion.

Fig. 7(c) shows the restitution coefficient ϵ, defined as ratio of the droplet center maximum height after first bouncing divided by the initial droplet centre height from the experiments described in Fig. 7(a). For the different mixture cases, the restitution coefficient is plotted vs. the sliding angle. The trend shows that when the sliding angle is at a certain critical value, the restitution coefficient is around 0. The restitution coefficient increases with lower sliding angle. In previous work, the restitution coefficient ϵ is reported to be related with the impact Weber number [77–79] at the complete rebound range, namely $\epsilon \sim (We)^{-0.25}$. Here, our restitution coefficient is strongly affected by the sliding angle at similar Weber numbers. This implies that the restitution coefficient is not only represented by the Weber number but also by the surface adhesion property (characterized by the sliding angle). The complete rebound happens when the surface adhesion is smaller than a certain value. During drop impact, the energy loss is from viscous dissipation and dissipation at the contact line. In these cases, as the

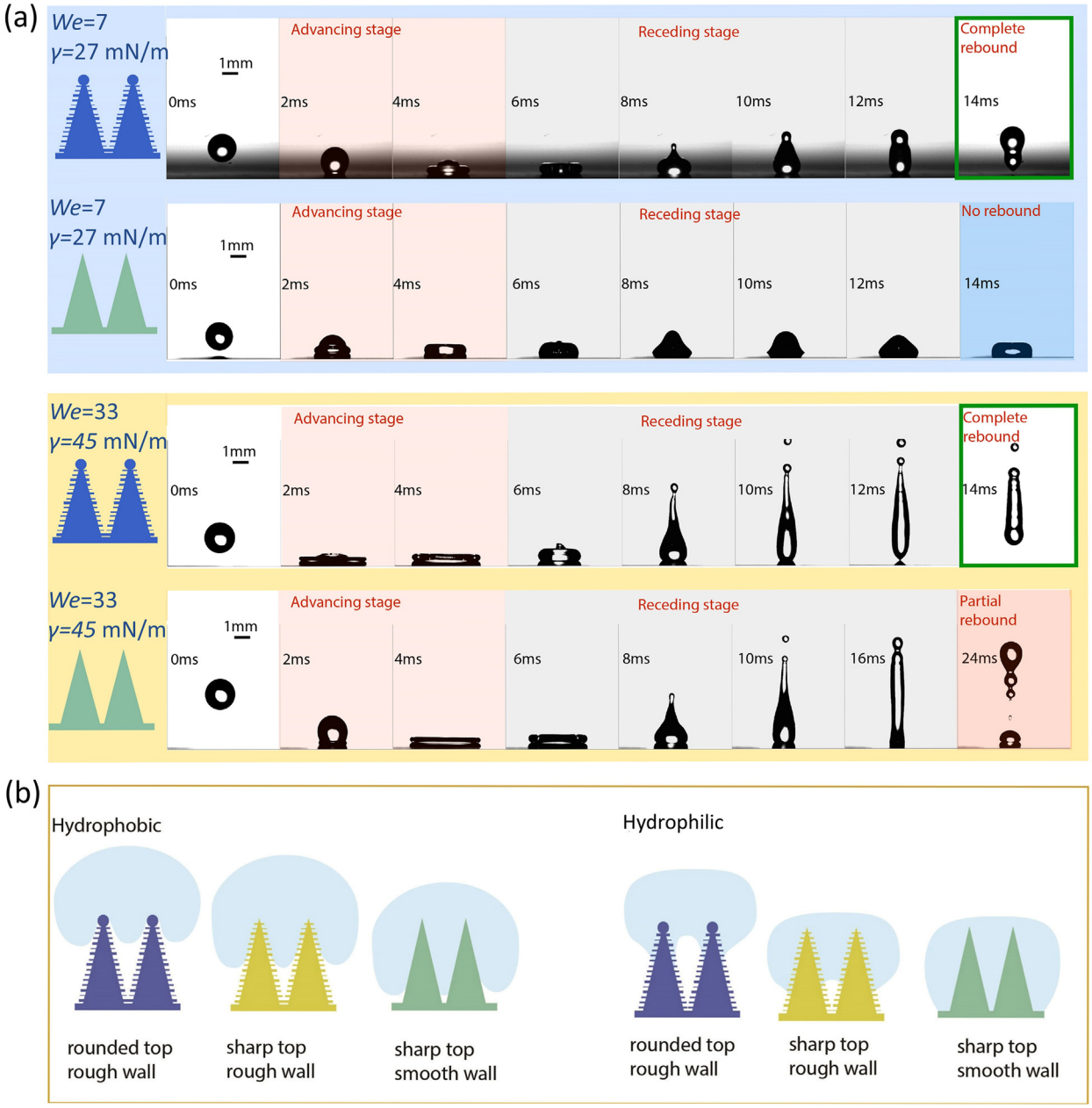

Fig. 6. (a) Selected droplet impact images are presented, red patch for advancing stage and gray patch for receding stage. In the first two rows, comparison of droplet impact for surface tension of 27 mN/m at similar impact velocity is shown. In last two rows, comparison of droplet impact for surface tension of 45 mN/m at similar impact velocity is presented. The samples are all with pitch 8 μm, SP8H20 without side wall roughness and RP8H27 with side wall roughness. (b) Illustration of possible solid–liquid contact at three conditions for smooth cones and cones with lateral roughness.

viscosity of ethanol/water mixture is changing in small amounts, we attribute the difference in restitution coefficient to the capillary force difference, which leads to difference of contact angle and adhesion property. This implies that the major energy dissipation difference is due to the difference of contact area or total triple line length. The lower sliding angle means lower threshold force for depinning, which also means the triple line overcomes less force while depinning.

Fig. 7(b) shows the wetted contact baseline diameter with time. We deposit droplets with different surface tension on surfaces RP8H27 and SP8H20 and record the process using the same setting as done in Fig. 7(a). The y-axis data ($D(t)$, contact baseline with time) is normalized by the maximum contact baseline (D_m), where the baseline data is obtained from image processing of the drop impact video. The two smooth cone cases (square symbol) have penetration and behave without complete rebound, while the three rough cone (circle symbol) cases display complete rebound. The ratio of initial droplet diameter D_0 and capillary length $\lambda = \sqrt{\frac{\Upsilon}{\rho g}}$ in these cases lies around 0.9–1.1 (not distinctly larger than 1), therefore we neglect gravity induced droplet deformation. Actually gravity effect is usually not considered as an important term for droplet impact phenomena [46].

In Fig. 7(b) all the contact baseline sizes at the advancing stage with time collapse into a similar curve, as also reported by other works [80,81]. The different contact angle cases here lie on a similar curve, which means that wettability effect is negligible. However, it is shown that the receding phase presents differences

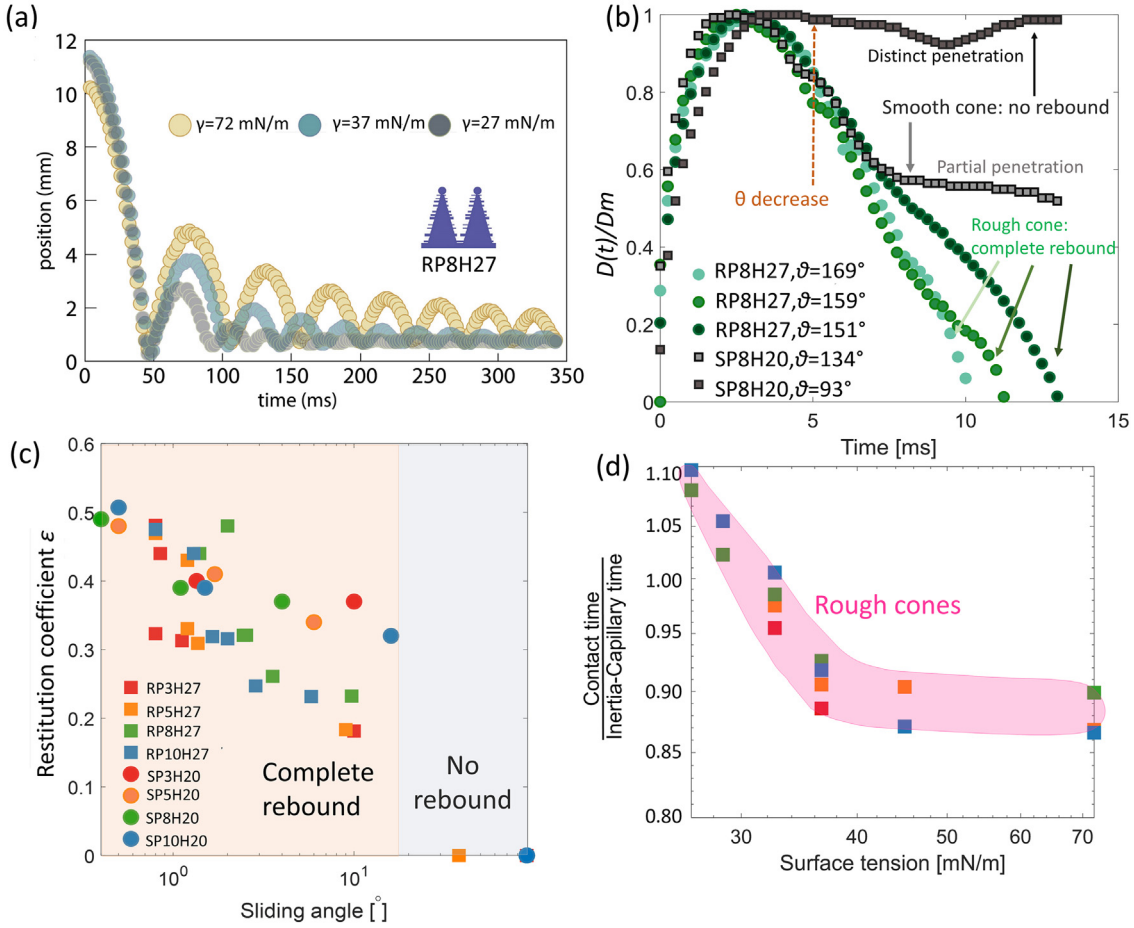

Fig. 7. In (a), comparison of droplet bouncing on cones RP8H27. Y-axis is the center vertical position of a droplet with time. Three different surface tension cases are presented, 72 mN/m, 37 mN/m and 27 mN/m. There is bouncing behavior difference at similar impact height, though it is all complete rebound. In (b), wetted contact base diameter normalized by maximum contact length is plotted. For surface RP8H27, pure water, θ = 169°, *We* = 6.6; drop with 33 mN/m (35% ethanol in volume), θ = 159°, *We* = 10.5; drop with 27 mN/m (67% ethanol in volume), θ = 151°, *We* = 9.6; It is shown that advancing phase is almost the same while the receding phase differs with time. For CP8H20 case, drop with 33 mN/m (35% ethanol in volume), θ = 134°, *We* = 10.5; drop with 27 mN/m (67% ethanol in volume), θ = 93°, *We* = 12.0; In (c), restitution coefficient vs. sliding angle at the same impact height (around 1 cm) is plotted. The restitution coefficient decreases with sliding angle. In (d), contact time divided by the inertia-capillary time ($\tau = 2.6\left(\frac{\rho R^3}{\gamma}\right)^{0.5}$) is plotted vs. surface tension on various rough conical surfaces at around 1 cm impact height.

between different cases in Fig. 7(b) from certain time. The lower contact angle case takes longer to retract. Taking the pure water case on rough cones as reference (light green circle symbol), the receding velocity is slowed down for all other cases, as shown in Fig. 7(b), where the slope of the position with time decreases. The deviation starts earlier when contact angle is lower on the same surface at similar impact conditions, which indicates that the reduction of capillary force results in lower driving force. In addition, based on the Cassie-Baxter model, lower contact angle implies higher solid–liquid contact fraction, thus more total triple line results in more energy dissipation at the triple line. For structured surfaces in the literature [41] or in current work, some of the $D(t)/D_m$ curves overlap during the receding stage. This overlapping phenomena cannot be explained by wettability only, as different wettability on the smooth surface shows deviation in the receding process [82,83]. Similar surface contact angle range is covered, namely 134°-157°, therefore the observed difference is not due to the contact angle range considered. On the smooth surface, there is full solid–liquid contact below the droplet while the existence of a structure can reduce the solid–liquid contact when in the Cassie state. The receding part can have certain overlapping when it is in partial Wenzel state or Cassie state. As shown in Fig. 7(b), the square symbol no-rebound case (contact angle 134°) still has some overlapping with the other green curves for complete rebound cases. We attribute this overlapping to liquid movement above the structure top. The spreading liquid does not wet all the structure below but only partially penetrates around the droplet center area due to the impact. When the liquid recedes above the structure top, the effect of the sidewall roughness is negligible.

Deng et al.'s work [41] reports slower receding when the baseline is around the initial droplet diameter D_0, using mixtures with different surface tension. They proposed [41] that the slower receding is due to temporal impalement. Recall that the viscosity difference is quite small in this work, thus the different contact behaviour is mainly ascribed to the difference of inertia and capillary force. As we observe differences here at similar impact velocities (inertia is similar), it is proposed that the impalement area varies due to differences in capillary force. The lower contact angle cases have larger temporal impalement area, as the deviation shown in Fig. 7(b) happens earlier for the rough cones cases. For instance, the rough cones case with static contact angle of 159° deviates from the 169° case at around 10 ms, while the 151° case deviates from the 169° case at around 7 ms. Here, we attribute the reason of impalement difference to the decrease of anti-wetting pressure due to lower surface tension. The peak pressure during drop impact can show a higher value in the centre and

lower value on the outside of the droplet base [84], therefore the local wetting pressure can be different and local penetration will differ.

In Fig. 7(d), the contact time of rough cones for different surface tension cases is plotted with the corresponding surface tension. The deposition height is kept at around 1 cm. The contact time is non-dimensionalized with inertia-capillary time scale $\tau = 2.6\left(\frac{\rho R^3}{\gamma}\right)^{0.5}$ [85]. We observe the effect of surface tension (especially for γ below 45 mN/m), namely the dimensionless contact time increases with decreasing surface tension, which is ascribed to lower capillary force resulting in more temporary impalement. In the hydrophobic range (for γ above 45 mN/m), the liquid tends to be repelled from the surface, therefore the surface tension effect is not distinct due to a lack of wetting induced impalement.

4. Conclusions

In this work, we present a method to add re-entrant like sidewall roughness all along micro-conical pillars. We conduct droplet impact experiments with liquids of different surface tension and report enhanced superamphiphobicity for this tree-branches like topography. The tree-branches like structures show better anti-wetting properties as compared to similar structures without lateral roughness. It is shown that the tree-branches like structures can enhance the anti-impalement ability and also reduce the adhesion properties (illustrated as sliding angle). The reduced solid–liquid contact and lower surface adhesion properties help to decrease the energy dissipation during droplet impact and the anti-wetting performance is improved. Although different types of structures have been proposed in the literature as optimum structures for superamphiphobic surfaces [63,64], these surfaces struggle to maintain their super-repellent properties at higher droplet impact velocities. We found that the superamphiphobicity is improved in this work compared with rigid surfaces at similar experimental conditions, reaching super-repellent conditions after droplet impact of low surface tension fluids for higher *We* numbers than previously reported in the literature [41,44,68,69]. Surfaces with higher anti-impalement ability and lower adhesion properties are desired for further improvement of superamphiphobicity.

CRediT authorship contribution statement

Wenwu Ding: Conceptualization of this study, Methodology, experiment, data analysis, Writing - Original draft preparation. **Carlos Alberto Dorao:** Methodology, data analysis, Writing - Original draft preparation. **Maria Fernandino:** Methodology, data analysis, Writing - Original draft preparation.

Declaration of Competing Interest

The authors declare that they have no known competing financial interests or personal relationships that could have appeared to influence the work reported in this paper.

Acknowledgments

The Research Council of Norway is acknowledged for the support to the Norwegian Micro- and Nano-Fabrication Facility, NorFab, project number 295864.

References

[1] Chien-Chih Huang, Martin Z. Bazant, Todd Thorsen, Ultrafast high-pressure AC electro-osmotic pumps for portable biomedical microfluidics, Lab Chip 10 (1) (2010) 80–85.
[2] Hartmann E. N'guessan, Aisha Leh, Paris Cox, Prashant Bahadur, Rafael Tadmor, Prabir Patra, Robert Vajtai, Pulickel M. Ajayan, Priyanka Wasnik, Water tribology on graphene, Nature Communications 3 (1) (2012) 1242.
[3] Robert J. Daniello, Nicholas E. Waterhouse, Jonathan P. Rothstein, Drag reduction in turbulent flows over superhydrophobic surfaces, Phys. Fluids 21 (8) (2009) 085103.
[4] Bharat Bhushan, Yong Chae Jung, Natural and biomimetic artificial surfaces for superhydrophobicity, self-cleaning, low adhesion, and drag reduction, Prog. Mater Sci. 56 (1) (2011) 1–108.
[5] Richard Truesdell, Andrea Mammoli, Peter Vorobieff, Frank van Swol, C. Jeffrey Brinker, Drag Reduction on a Patterned Superhydrophobic Surface, Phys. Rev. Lett. 97 (4) (2006) 044504.
[6] Choongyeop Lee, Chang-Jin Kim, Underwater Restoration and Retention of Gases on Superhydrophobic Surfaces for Drag Reduction, Phys. Rev. Lett. 106 (1) (2011) 014502.
[7] Xi Yao, Qinwen Chen, Xu. Liang, Qikai Li, Yanlin Song, Xuefeng Gao, David Quéré, Lei Jiang, Bioinspired Ribbed Nanoneedles with Robust Superhydrophobicity, Adv. Funct. Mater. 20 (4) (2010) 656–662.
[8] Shunsuke Nishimoto, Bharat Bhushan, Bioinspired self-cleaning surfaces with superhydrophobicity, superoleophobicity, and superhydrophilicity, RSC Adv. 3 (3) (2013) 671–690.
[9] Kesong Liu, Lei Jiang, Bio-Inspired Self-Cleaning Surfaces, Annu. Rev. Mater. Res. 42 (1) (2012) 231–263.
[10] Ralf Blossey, Self-cleaning surfaces – virtual realities, Nat. Mater. 2 (5) (2003) 301–306.
[11] Lu. Yao, Sanjayan Sathasivam, Jinlong Song, Colin R. Crick, Claire J. Carmalt, Ivan P. Parkin, Robust self-cleaning surfaces that function when exposed to either air or oil, Science 347 (6226) (2015) 1132–1135.
[12] William S.Y. Wong, Guanyu Liu, Noushin Nasiri, Chonglei Hao, Zuankai Wang, Antonio Tricoli, Omnidirectional Self-Assembly of Transparent Superoleophobic Nanotextures, ACS Nano 11 (1) (2017) 587–596.
[13] Shuaijun Pan, Arun K. Kota, Joseph M. Mabry, Anish Tuteja, Superomniphobic Surfaces for Effective Chemical Shielding, J. Am. Chem. Soc. 135 (2) (2013) 578–581.
[14] Jiale Yong, Feng Chen, Qing Yang, Jinglan Huo, Xun Hou, Superoleophobic surfaces, Chem. Soc. Rev. 46 (14) (2017) 4168–4217.
[15] Lu. Xuemei, Yuelian Peng, Haoran Qiu, Xinrui Liu, Lei Ge, Anti-fouling membranes by manipulating surface wettability and their anti-fouling mechanism, Desalination 413 (2017) 127–135.
[16] A.J. Scardino, H. Zhang, D.J. Cookson, R.N. Lamb, R. de Nys, The role of nano-roughness in antifouling, Biofouling 25 (8) (2009) 757–767.
[17] Jin Yang, Zhaozhu Zhang, Xu. Xianghui, Xuehu Men, Xiaotao Zhu, Xiaoyan Zhou, Superoleophobic textured aluminum surfaces, New J. Chem. 35 (11) (2011) 2422.
[18] Hua Jin, Marjo Kettunen, Ari Laiho, Hanna Pynnonen, Jouni Paltakari, Abraham Marmur, Olli Ikkala, Robin H.A. Ras, Superhydrophobic and Superoleophobic Nanocellulose Aerogel Membranes as Bioinspired Cargo Carriers on Water and Oil, Langmuir 27 (5) (2011) 1930–1934.
[19] Yuzhang Zhu, Dong Wang, Lei Jiang, Jian Jin, Recent progress in developing advanced membranes for emulsified oil/water separation, NPG Asia Materials 6 (5) (2014). e101–e101.
[20] Amir Razmjou, Ellen Arifin, Guangxi Dong, Jaleh Mansouri, Vicki Chen, Superhydrophobic modification of TiO2 nanocomposite PVDF membranes for applications in membrane distillation, J. Membr. Sci. 415–416 (2012) 850–863.
[21] Ziqi Sun, Ting Liao, Kesong Liu, Lei Jiang, Jung Ho Kim, Shi Xue Dou, Fly-Eye Inspired Superhydrophobic Anti-Fogging Inorganic Nanostructures, Small 10 (15) (2014) 3001–3006.
[22] Matt W. England, Tomoya Sato, Chihiro Urata, Liming Wang, Atsushi Hozumi, Transparent gel composite films with multiple functionalities: Long-lasting anti-fogging, underwater superoleophobicity and anti-bacterial activity, J. Colloid Interface Sci. 505 (2017) 566–576.
[23] Mingjie Liu, Shutao Wang, Lei Jiang, Nature-inspired superwettability systems, Nature Reviews Materials 2 (7) (2017) 17036.
[24] Jeong-Gil Kim, Hyungryul J. Choi, Kyoo-Chul Park, Robert E. Cohen, Gareth H. McKinley, George Barbastathis, Multifunctional Inverted Nanocone Arrays for Non-Wetting, Self-Cleaning Transparent Surface with High Mechanical Robustness, Small 10 (12) (2014) 2487–2494.
[25] Liangliang Cao, Andrew K. Jones, Vinod K. Sikka, Wu. Jianzhong, Di Gao, Anti-Icing Superhydrophobic Coatings, Langmuir 25 (21) (2009) 12444–12448.
[26] Peng Guo, Yongmei Zheng, Mengxi Wen, Cheng Song, Yucai Lin, Lei Jiang, Icephobic/Anti-Icing Properties of Micro/Nanostructured Surfaces, Adv. Mater. 24 (19) (2012) 2642–2648.
[27] Xuemei Chen, Wu. Jun, Ruiyuan Ma, Meng Hua, Nikhil Koratkar, Shuhuai Yao, Zuankai Wang, Nanograssed Micropyramidal Architectures for Continuous Dropwise Condensation, Adv. Funct. Mater. 21 (24) (2011) 4617–4623.
[28] Nenad Miljkovic, Ryan Enright, Youngsuk Nam, Ken Lopez, Nicholas Dou, Jean Sack, Evelyn N. Wang, Jumping-Droplet-Enhanced Condensation on Scalable Superhydrophobic Nanostructured Surfaces, Nano Lett. 13 (1) (2013) 179–187.
[29] Konrad Rykaczewski, Adam T. Paxson, Matthew Staymates, Marlon L. Walker, Xiaoda Sun, Sushant Anand, Siddarth Srinivasan, Gareth H. McKinley, Jeff Chinn, John Henry J. Scott, Kripa K. Varanasi, Dropwise condensation of low surface tension fluids on omniphobic surfaces, Scientific Reports 4 (1) (2014) 1–8.
[30] Kosmas Ellinas, Angeliki Tserepi, Evangelos Gogolides, Durable superhydrophobic and superamphiphobic polymeric surfaces and their applications: A review, Adv. Colloid Interface Sci. 250 (2017) 132–157.

[31] Chaoyi Peng, Zhuyang Chen, and Manish K. Tiwari. All-organic superhydrophobic coatings with mechanochemical robustness and liquid impalement resistance. Nature Materials 2018 17:4, 17(4):355–360, 2018.
[32] Anish Tuteja, Wonjae Choi, Minglin Ma, Joseph M Mabry, Sarah A Mazzella, Gregory C Rutledge, Gareth H McKinley, Robert E Cohen, Designing superoleophobic surfaces, Science (New York, N.Y.) 318 (5856) (2007) 1618–1622.
[33] A. Tuteja, W. Choi, J.M. Mabry, G.H. McKinley, R.E. Cohen, Robust omniphobic surfaces, Proc. Nat. Acad. Sci. 105 (47) (2008) 18200–18205.
[34] Bo Zhang, Xianren Zhang, Elucidating Nonwetting of Re-Entrant Surfaces with Impinging Droplets, Langmuir 31 (34) (2015) 9448–9457.
[35] Shuaijun Pan, Rui Guo, Mattias Björnmalm, Joseph J. Richardson, Ling Li, Chang Peng, Nadja Bertleff-Zieschang, Xu. Weijian, Jianhui Jiang, Frank Caruso, Coatings super-repellent to ultralow surface tension liquids, Nat. Mater. 17 (11) (2018) 1040–1047.
[36] Philip S. Brown, Bharat Bhushan, Durable, superoleophobic polymer-nanoparticle composite surfaces with re-entrant geometry via solvent-induced phase transformation, Scientific Reports 6 (1) (2016) 21048.
[37] Xuemei Chen, Justin A. Weibel, Suresh V. Garimella, Characterization of Coalescence-Induced Droplet Jumping Height on Hierarchical Superhydrophobic Surfaces, ACS Omega 2 (6) (2017) 2883–2890.
[38] Wu. Yi, Jing Zeng, Yinsong Si, Min Chen, Wu. Limin, Large-Area Preparation of Robust and Transparent Superomniphobic Polymer Films, ACS Nano 12 (10) (2018) 10338–10346.
[39] Min Xi, Jiale Yong, Feng Chen, Qing Yang, Xun Hou, A femtosecond laser-induced superhygrophobic surface: beyond superhydrophobicity and repelling various complex liquids, RSC Advances 9 (12) (2019) 6650–6657.
[40] Hyunchul Kim, Heetak Han, Sanggeun Lee, Janghoon Woo, Jungmok Seo, Taeyoon Lee, Nonfluorinated Superomniphobic Surfaces through Shape-Tunable Mushroom-like Polymeric Micropillar Arrays, ACS Applied Materials and Interfaces 11 (5) (2019) 5484–5491.
[41] Xu Deng, Frank Schellenberger, Periklis Papadopoulos, Doris Vollmer, Hans Jürgen Butt, Liquid drops impacting superamphiphobic coatings, Langmuir 29 (25) (2013) 7847–7856.
[42] Shuantao Dong, Yabin Li, Ning Tian, Bucheng Li, Yanfei Yang, Lingxiao Li, Junping Zhang, Scalable Preparation of Superamphiphobic Coatings with Ultralow Sliding Angles and High Liquid Impact Resistance, ACS Applied Materials and Interfaces 10 (49) (2018) 41878–41882.
[43] Kosmas Ellinas, Marianneza Chatzipetrou, Ioanna Zergioti, Angeliki Tserepi, Evangelos Gogolides, Superamphiphobic Polymeric Surfaces Sustaining Ultrahigh Impact Pressures of Aqueous High- and Low-Surface-Tension Mixtures, Tested with Laser-Induced Forward Transfer of Drops, Adv. Mater. 27 (13) (2015) 2231–2235.
[44] Seunghyeon Baek, Hyun Sik Moon, Wuseok Kim, Sangmin Jeon, Kijung Yong, Effect of liquid droplet surface tension on impact dynamics over hierarchical nanostructure surfaces, Nanoscale 10 (37) (2018) 17842–17851.
[45] William S.Y. Wong, Surface Chemistry Enhancements for the Tunable Super-Liquid Repellency of Low-Surface-Tension Liquids, Nano Lett. 19 (3) (2019) 1892–1901.
[46] A.L. Yarin, Drop impact dynamics: Splashing, Spreading, Receding, Bouncing, Annu. Rev. Fluid Mech. 38 (1) (2006) 159–192.
[47] William S.Y. Wong, Surface Chemistry Enhancements for the Tunable Super-Liquid Repellency of Low-Surface-Tension Liquids, Nano Lett. 19 (3) (2019) 1892–1901.
[48] Paul Calvert, Inkjet Printing for Materials and Devices, Chem. Mater. 13 (10) (2001) 3299–3305.
[49] John Kettle, Taina Lamminmäki, Patrick Gane, A review of modified surfaces for high speed inkjet coating, Surf. Coat. Technol. 204 (12–13) (2010) 2103–2109.
[50] Shuoran Chen, Su. Meng, Cong Zhang, Meng Gao, Bin Bao, Qiang Yang, Su. Bin, Yanlin Song, Fabrication of Nanoscale Circuits on Inkjet-Printing Patterned Substrates, Adv. Mater. 27 (26) (2015) 3928–3933.
[51] Berend-Jan de Gans, Ulrich S. Schubert, Inkjet Printing of Well-Defined Polymer Dots and Arrays, Langmuir 20 (18) (2004) 7789–7793.
[52] Bong Kyun Park, Dongjo Kim, Sunho Jeong, Jooho Moon, Jang Sub Kim, Direct writing of copper conductive patterns by ink-jet printing, Thin Solid Films 515 (19 SPEC. ISS.) (2007) 7706–7711.
[53] Collin Ladd, Ju-Hee So, John Muth, Michael D. Dickey, 3D Printing of Free Standing Liquid Metal Microstructures, Adv. Mater. 25 (36) (2013) 5081–5085.
[54] Andreas Carlson, Gabriele Bellani, Gustav Amberg, Universality in dynamic wetting dominated by contact-line friction, Physical Review E - Statistical, Nonlinear, and Soft Matter Physics 85 (4) (2012) 045302.
[55] Yuli Wang, Gustav Amberg, Andreas Carlson, Local dissipation limits the dynamics of impacting droplets on smooth and rough substrates, Physical Review Fluids 2 (3) (2017) 033602.
[56] Daniel Bonn, Jens Eggers, Joseph Indekeu, Jacques Meunier, Wetting and spreading, Rev. Mod. Phys. 81 (2) (2009) 739–805.
[57] C. Frankiewicz, D. Attinger, Texture and wettability of metallic lotus leaves, Nanoscale 8 (7) (2016) 3982–3990.
[58] Matthew McCarthy, Konstantinos Gerasopoulos, Ryan Enright, James N. Culver, Reza Ghodssi, Evelyn N. Wang, Biotemplated hierarchical surfaces and the role of dual length scales on the repellency of impacting droplets, Appl. Phys. Lett. 100 (26) (2012) 263701.
[59] W. Ding, M. Fernandino, C.A. Dorao, Conical micro-structures as a route for achieving super-repellency in surfaces with intrinsic hydrophobic properties, Appl. Phys. Lett. 115 (5) (2019) 053703.
[60] Philippe Bourrianne, Cunjing Lv, David Quéré, The cold Leidenfrost regime, Science Advances 5 (6) (2019) eaaw0304.
[61] Kyoo Chul Park, Hyungryul J. Choi, Chih Hao Chang, Robert E. Cohen, Gareth H. McKinley, George Barbastathis, Nanotextured silica surfaces with robust superhydrophobicity and omnidirectional broadband supertransmissivity, ACS Nano 6 (5) (2012) 3789–3799.
[62] Ted Mao, David C.S. Kuhn, Honghi Tran, Spread and Rebound of Liquid Droplets upon Impact on Flat Surfaces, AIChE J. 43 (9) (1997) 2169–2179.
[63] Gene Whyman, Edward Bormashenko, How to make the cassie wetting state stable?, Langmuir 27 (13) (2011) 8171–8176
[64] Hans Jürgen Butt, Ciro Semprebon, Periklis Papadopoulos, Doris Vollmer, Martin Brinkmann, Matteo Ciccotti, Design principles for superamphiphobic surfaces, Soft Matter 9 (2) (2013) 418–428.
[65] Jinlin Zhang, Hong Zhao, Pinning and wetting stability of liquids on superoleophobic textured surfaces, Surface Innovations 2 (2) (2014) 103–115.
[66] Jinlong Song, Shuai Huang, Hu. Ke, Lu. Yao, Xin Liu, Xu. Wenji, Fabrication of superoleophobic surfaces on Al substrates, Journal of Materials Chemistry A 1 (46) (2013) 14783.
[67] René Hensel, Ralf Helbig, Sebastian Aland, Hans Georg Braun, Axel Voigt, Christoph Neinhuis, Carsten Werner, Wetting resistance at its topographical limit: The benefit of mushroom and serif T structures, Langmuir 29 (4) (2013) 1100–1112.
[68] Longquan Chen, Zhiyong Xiao, Philip C.H. Chan, Yi Kuen Lee, and Zhigang Li. A comparative study of droplet impact dynamics on a dual-scaled superhydrophobic surface and lotus leaf, Appl. Surf. Sci. 257 (21) (2011) 8857–8863.
[69] Peichun Tsai, Sergio Pacheco, Christophe Pirat, Leon Lefferts, Detlef Lohse, Drop impact upon micro- and nanostructured superhydrophobic surfaces, Langmuir 25 (20) (2009) 12293–12298.
[70] Wei Fang, Hao Yuan Guo, Bo Li, Qunyang Li, Xi Qiao Feng, Revisiting the Critical Condition for the Cassie-Wenzel Transition on Micropillar-Structured Surfaces, Langmuir 34 (13) (2018) 3838–3844.
[71] G. Pashos, G. Kokkoris, A.G. Boudouvis, A modified phase-field method for the investigation of wetting transitions of droplets on patterned surfaces, J. Comput. Phys. 283 (2015) 258–270.
[72] George Pashos, George Kokkoris, Andreas G. Boudouvis, Minimum Energy Paths of Wetting Transitions on Grooved Surfaces, Langmuir 31 (10) (2015) 3059–3068.
[73] G. Pashos, G. Kokkoris, A.G. Papathanasiou, A.G. Boudouvis, Wetting transitions on patterned surfaces with diffuse interaction potentials embedded in a Young-Laplace formulation, J. Chem. Phys. 144 (3) (2016). 034105–034105.
[74] C.W. Extrand*, Model for Contact Angles and Hysteresis on Rough and Ultraphobic Surfaces, Langmuir 18 (21) (2002) 7991–7999.
[75] Tingyi Liu, Chang Jin Kim, Turning a surface superrepellent even to completely wetting liquids, Science 346 (6213) (2014) 1096–1100.
[76] Shaoxian Song, Changsheng Peng, Viscosities of Binary and Ternary Mixtures of Water, Alcohol, Acetone, and Hexane, J. Dispersion Sci. Technol. 29 (10) (2008) 1367–1372.
[77] Christophe Clanet, Cédric Béguin, Denis Richard, David Quéré, Maximal deformation of an impacting drop, J. Fluid Mech. 517 (2004) 199–208.
[78] Adrianus I. Aria, Morteza Gharib, Physicochemical characteristics and droplet impact dynamics of superhydrophobic carbon nanotube arrays, Langmuir 30 (23) (2014) 6780–6790.
[79] Damon G.K. Aboud, Anne Marie Kietzig, On the Oblique Impact Dynamics of Drops on Superhydrophobic Surfaces. Part II: Restitution Coefficient and Contact Time, Langmuir 34 (34) (2018) 9889–9896.
[80] D.C. Vadillo, A. Soucemarianadin, C. Delattre, D.C.D. Roux, Dynamic contact angle effects onto the maximum drop impact spreading on solid surfaces, Phys. Fluids 21 (12) (2009) 1–8.
[81] Azar Alizadeh, Vaibhav Bahadur, Sheng Zhong, Wen Shang, Ri Li, James Ruud, Masako Yamada, Liehui Ge, Ali Dhinojwala, Manohar Sohal, Temperature dependent droplet impact dynamics on flat and textured surfaces, Appl. Phys. Lett. 100 (11) (2012) 11601.
[82] Ilker S. Bayer, Constantine M. Megaridis, Contact angle dynamics in droplets impacting on flat surfaces with different wetting characteristics, J. Fluid Mech. 558 (2006) 415.
[83] M. Pasandideh-Fard, Y.M. Qiao, S. Chandra, J. Mostaghimi, Capillary effects during droplet impact on a solid surface, Phys. Fluids 8 (1996) 650.
[84] Choongyeop Lee, Youngsuk Nam, Henri Lastakowski, Janet I. Hur, Seungwon Shin, Anne Laure Biance, Christophe Pirat, Chang Jin Kim, Christophe Ybert, Two types of Cassie-to-Wenzel wetting transitions on superhydrophobic surfaces during drop impact, Soft Matter 11 (23) (2015) 4592–4599.
[85] Denis Richard, Christophe Clanet, David Quéré, Contact time of a bouncing drop, Nature 417 (6891) (2002). 811–811.